# Analysis of the Effects of Differently Shaped Embankments on the Density Current

Koue, Jinichi

(Citation)
Water,16(23):3369

(Issue Date)
2024-12

(Resource Type)
journal article

(Version)
Version of Record

water

MDPI

*Article*

# Analysis of the Effects of Differently Shaped Embankments on the Density Current

**Jinichi Koue**

Graduate School of Maritime Sciences, Kobe University, 5-1-1 Fukaeminami, Higashinada-ku, Kobe 658-0022, Japan; koue@maritime.kobe-u.ac.jp

**Abstract:** Density currents, fluid flows driven by differences in density, play a crucial role in disaster prevention for water pollution and tsunami mitigation, particularly due to thermal releases from power plants. Understanding their dynamics is pivotal for effective mitigation strategies. While the influence of seabed and lake bottom topography on density currents is well-studied, research on how embankment shapes affect these currents has been limited. This study aimed to fill this gap by experimentally and numerically analyzing the flow dynamics of density currents using various embankment shapes in a controlled water tank environment. The findings revealed distinct variations in density perturbation across different embankment shapes. Specifically, density currents exhibited reduced head velocities in embankments shaped as right-angled triangles, rectangles, and L-shapes, in that sequential order. This research underscores the significance of embankment design in modifying density currents, offering valuable insights for optimizing disaster management strategies related to water pollution and tsunami hazards induced by thermal effluents from industrial sources.

**Keywords:** density current; embankment shape; disaster prevention; lock-exchange problem; flow field analysis



**Citation:** Koue, J. Analysis of the Effects of Differently Shaped Embankments on the Density Current. *Water* **2024**, *16*, 3369. https://doi.org/10.3390/w16233369

Academic Editors: Ming He, Can Yang and Ruijia Jin

Received: 27 September 2024
Revised: 18 November 2024
Accepted: 20 November 2024
Published: 23 November 2024



## 1. Introduction

Density currents, which are flows generated by density differences between fluids, are a naturally occurring phenomenon in the atmosphere and oceans and can also be generated artificially [1]. Examples of naturally occurring density currents include the flow generated by the salinity difference between oceans and rivers in brackish waters, sea-land winds caused by the temperature difference between sea and land [2], snowmelt flowing from rivers into lakes, and sea water run-up caused by tsunamis [3]. Brackish water areas are prone to plankton blooms, and it is a challenge to predict how extensive their extent is [4]. In addition, snowmelt water with high oxygen content is expected to improve the hypoxia of the lake bottom in Lake Biwa, and one of the challenges is to understand the propagation of snowmelt water when it flows from the river into the lake [5]. Examples of artificially generated density currents include thermal effluent discharged from power stations into the ocean [6,7], oil spills from tankers [8], and atmospheric flows generated by the temperature difference between urban and suburban areas due to the heat island effect [9]. There is concern that warm water discharged from power stations can increase the growth of plankton, which in turn increases the number of fish species feeding on it, affecting aquaculture farms and fisheries. Knowing the spread of warm drainage and its behavior is therefore an important issue for those involved in the fishing industry [3]. Thus, analyzing the head structure in order to understand the behavior of density currents is one of the key issues in the field of the environment.

A basic model for studying the behavior of the density currents is the lock-exchange problem and numerous experiments [10–13] and numerical [14–16] studies have been conducted. In water tank experiments, a vertical partition plate (gate) is placed in the channel of a horizontal tank, and fluids of different densities are placed on both sides of the

gate. The density current is then generated by removing the gate, and the travelling velocity and mixing of the two fluids are analyzed. These experiments have been carried out with a flat bottom surface of the tank, but the bottoms of oceans and lakes have complex shapes and have a significant influence on ocean currents and lake flows. Furthermore, this is an important issue in considering how to control tsunami run-up, by means of embankments with different bottom shapes. Various theoretical [17] and experimental [18] studies have been conducted on wave dissipation caused by embankments, including vegetation and other natural embankments. Obstacles resembling vegetation have been implemented in experimental tanks and computational domains, and the behavior of density currents as they flow between and over the obstacles has been analyzed [19]. However, relatively few studies have investigated density currents focusing on the shape of the bottom surface.

The aim of this study is to clarify how the structure and mechanical mechanism of the head of the density current is affected by the shape of the bottom surface, which simulates the shape of real oceans and lakes, and how the phenomena change as a result. The clarification of these phenomena can contribute to proposing various phenomena of density currents and their suppression methods in real waters. Specifically, the density current field in a flow path with different tank bottom geometries is analyzed via tank experiments and numerical calculations. In the tank experiment, an embankment is placed on the side into which the fluid flows, and the flow of fluid of different densities colored with red food color is visualized and the density and velocity distributions are compared and investigated through image analysis. In numerical calculations, the equation of continuity for incompressible fluids, the transport equation for density, and the Navier-Stokes equation are solved via the finite volume method.

## 2. Methodology

### *2.1. Experimental Methods*

Figure 1 shows a schematic diagram of the experimental water tank. The water tank was made of acrylic, with an internal length (L) of 2000 mm, width (B) of 100 mm, and depth (H) of 100 mm. The thickness of the water tank was 10 mm, and the gate was placed at L/2 = 1000 mm from one side of the tank to partition the two fluids. The thickness of the gate was 3 mm. The water tank had a groove for the gate to fit into, and the gate was opened by sliding the gate upwards.

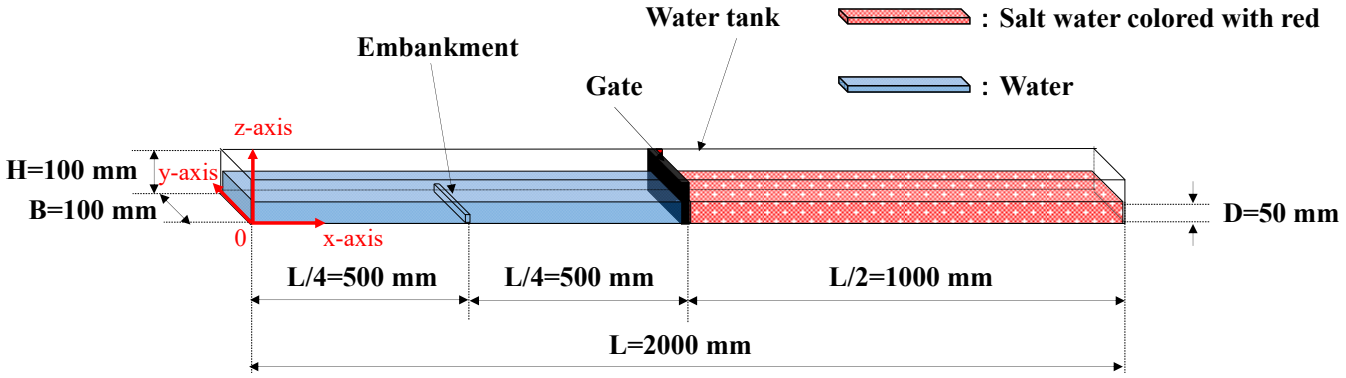


**Figure 1.** Schematic diagram of experiment.

An embankment was placed on one side of the water tank. The geometry of the embankment is shown in Figure 2. The embankments had three different cross-sectional shapes: rectangular, right-angled triangle, and L-shaped. The height of the embankments was 25 mm. The material was also manufactured from the same acrylic as the water tank.

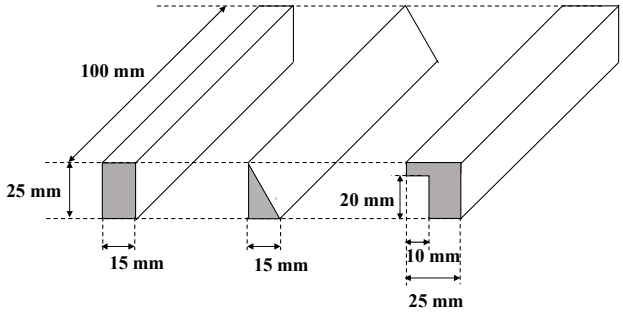


**Figure 2.** The shape of embankments (rectangular, right-angled triangle, and L-shaped).

The experiment was conducted by filling the side of the tank without the embankment with saltwater colored with red and filling the side of the embankment with water to a height D = 50 mm. The density of the water was represented by $\rho_0$, and the density of the initial brine was represented by $\rho_0 + \Delta\rho$. In this experiment, the density difference $\Delta\rho/\rho$ was 0.02.

The experiment was conducted with one embankment placed at a distance of L/4 = 500 mm from the gate. Filming was carried out from the side and top of the water tank, with a video camera in the vicinity of the embankment and on the side where the embankment was placed, respectively. On the other side where the video camera was placed, a blank piece of paper was attached to provide a white background.

### *2.2. Optical Arrangement*

First, the video footage captured by the camera was decomposed into individual frames. The position of the optics and camera used in the experiment depended on the position of the image and is shown in Figure 3. The frame rate of the video camera was 30 fps, and the pixel count was 12 megapixels.

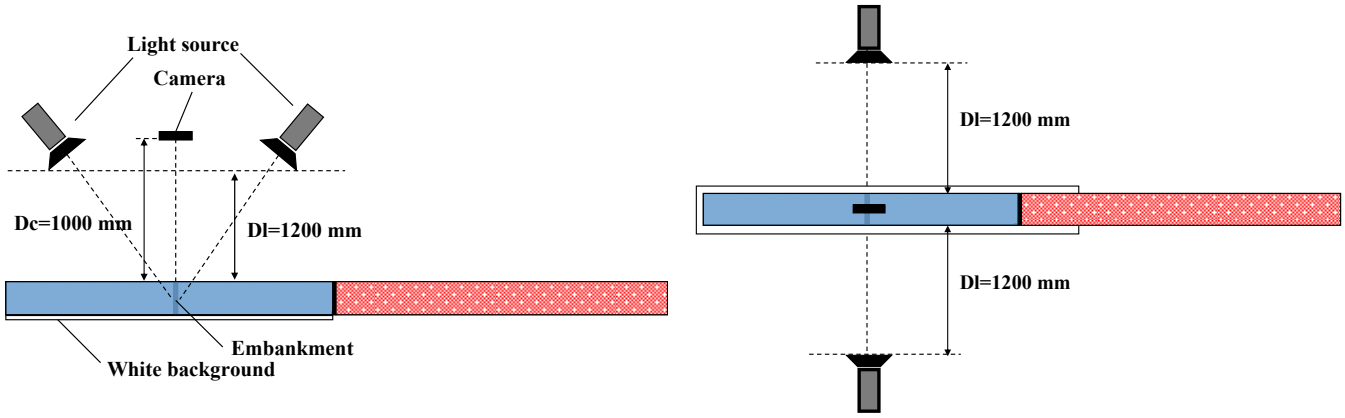


(**a**) (**b**)

**Figure 3.** Location of the optical system; (**a**) the condition photographed from the lateral side; (**b**) the condition photographed from the upper side.

## 3. Image Visualization Method

### *3.1. Image Analysis Method*

In order to obtain the density distribution from the video image of the experiment, a density field analysis was carried out by determining and utilizing the luminance values of the image. When light passes through a fluid colored with red, part of the light is absorbed, and the luminance value of the image becomes smaller. Using the fact that the amount of light absorbed changes with the density of the saltwater, the density of saltwater is measured from the image luminance value. When molecular diffusion is negligible, the

density of the saltwater corresponds to the density of the brine, so the density field can be determined from the image luminance values.

First, the video footage captured by the camera was decomposed into images that were sectioned into images. The area near the embankment was then trimmed to 200 × 800 pixels. The RGB values with each pixel in the image were captured, and the luminance value I was obtained; the conversion from RGB to luminance value I was calculated as in Equation (1) [20].

$$I = 0.3R + 0.59G + 0.11B \quad (1)$$

The range of luminance values I is $0 \leq I \leq 255$. A median filter was used to remove noise due to light reflections on the tank wall and other factors. The median filter outputs the median value of the pixels in the filter as the representative value, thus smoothing the image and removing outliers. The size of the median filter was 7 × 7 pixels. An image with water in the same position and with the same optics as the shooting point was prepared as the background image, and the difference ΔI between the luminance value $I_0$ of the background image and the luminance value I of the image to be analyzed was taken.

$$\Delta I = I_0 - I \quad (2)$$

The difference $\Delta I_{max}$ between the luminance value $l_{brine}$ in the brine side before the sluice was opened and the luminance value $I_0$ in the background image was calculated, and the value of density was made dimensionless by dividing ΔI by $\Delta I_{max}$. The dimensionless density is denoted as $\rho_s$.

$$\Delta I_{max} = I_0 - I_{brine} \quad (3)$$

$$\rho_s = \frac{\Delta I}{\Delta I_{max}} \quad (4)$$

### 3.2. Measurement of Head Position of the Density Current

The head position was measured from an image trimmed from a video of the entire density current from the top of the water tank. Figure 4 shows the method of measuring the head position of the density current. As in the density measurement, the video was cut into images, and the water tank area was trimmed. The RGB value of each pixel in the trimmed image was read, and the head position was defined as the position where the R-value was more than half the R-value of the brine colored with red before the gate was opened (initial condition). As the background is white here, the R-value of the background should be zero. As the RGB values of the white background each have high values, the R-values of pixels with B and G values above 150 were set to zero so that the background image would not affect the head position.

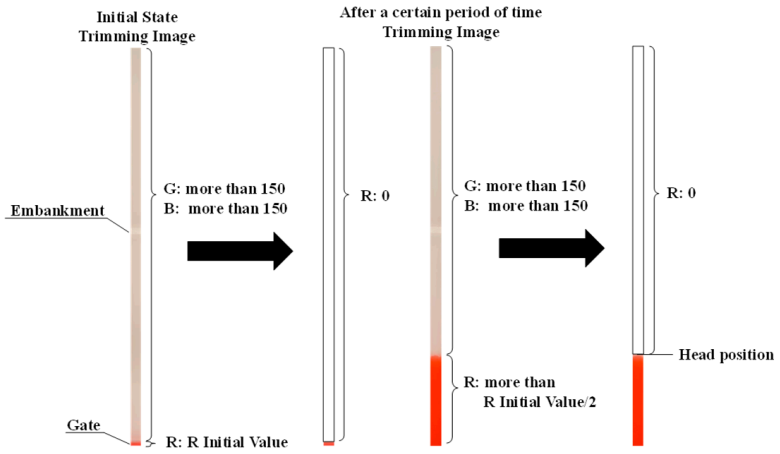


**Figure 4.** Method of measuring the head position of the density current.

## 4. Numerical Simulations

Numerical simulations were carried out in two dimensions to analyze the behavior of density current propagation with respect to the bottom embankment in the water tank experiment. The water tank was divided into an 800 × 20 square grid, and the conditions of continuity of the incompressible fluid and the transport and Navier–Stokes equations of density were solved via the finite volume method. The governing equations are presented in Equations (5)–(7).

$$\nabla \cdot u = 0 \tag{5}$$

$$\frac{\partial \rho_s}{\partial t} + \nabla \cdot (\rho_s u) = Rs^{-1} \nabla^2 \rho_s \tag{6}$$

$$\frac{\partial (\rho u)}{\partial t} + \nabla \cdot (\rho u u) = -\nabla \phi + Re^{-1} \nabla^2 u - \rho_s Fn^{-2} k \tag{7}$$

where u is the velocity vector of the medium, ϕ is the change in pressure with respect to the hydrostatic pressure of the medium, and k is the vertical upward unit vector along the z axis.

All variables are non-dimensionalized here with water depth D and representative velocity U. The representative velocity U is given by Equation (8)

$$U = \sqrt{g' D} \tag{8}$$

$$g' = \frac{\Delta \rho}{\rho_0} g \tag{9}$$

where $g'$ is the acceleration representing the real effect of the density difference. The representative time T is imposed as the following equation:

$$T = \frac{D}{U} = \frac{D}{\sqrt{g' D}} = \sqrt{\frac{D}{g'}} \tag{10}$$

The medium diffusion parameters Rs, Reynolds number Re, and Froude number Fr are imposed as follows:

$$Rs = \frac{UD}{\kappa} \tag{11}$$

$$Re = \frac{UD}{\nu} \tag{12}$$

$$Fr = \frac{U}{\sqrt{g' D}} \tag{13}$$

where $\kappa$ is the molecular diffusion coefficient of the medium, and $\nu$ is the kinematic viscosity coefficient of the fluid.

At the wall and embankment boundaries, a condition is imposed where the diffusion velocity of the medium is zero, and a no-slip condition is imposed for the velocity. The velocity inside the corner of the embankment was assumed to be zero.

$$n \cdot \nabla \rho_s = 0 \tag{14}$$

$$u = 0 \tag{15}$$

$$u_n = 0 \tag{16}$$

$$n \cdot \nabla u_t = 0 \tag{17}$$

where n is the unit normal vector of the wall surface, and $u_n$ and $u_t$ are the normal and tangential components at the wall surface of the respective velocity. The initial conditions are that the fluid in the channel of length L and depth D, $0 \leq x \leq L$, and $0 \leq z \leq D$ is

stationary with the left end of the channel x = 0 to the gate x = L/2 and is filled with fluid of density $\rho_0$ and the remaining part $L/2 \leq x \leq L$ with a fluid of density $\rho_0 + \Delta\rho$.

The initial conditions are as follows:

$$u = 0 \tag{18}$$

$$\rho_s = \begin{cases} 0 & 0 \leq x \leq L/2 \\ 1 & L/2 \leq x \leq L \end{cases} \tag{19}$$

The pressure field corresponding to the density field given by the staircase function is for open channels,

$$\phi = \begin{cases} 0 & 0 \leq x \leq L/2 \\ -Fn^{-2}k & L/2 \leq x \leq L \end{cases} \tag{20}$$

The function is continuous in the upper plane z = D as in Equation (20). The governing equations in Equations (2)–(4) are expanded into components of the Cartesian coordinate system and discretized based on the finite volume method. The components of the velocity vector are also staggered at the center of the cell surface, while pressure and density are defined at the center of the cell. The spatial derivatives in the governing equations are approximated by a second-order accurate central difference. The values at points in space other than the defining point are evaluated via the arithmetic mean of the values at neighboring defining points. The convection term in the density transport Equation (3) is approximated via the donor cell method and the QUICK method in addition to the central difference. The second term on the right-hand side of Equation (3) is approximated via the donor cell method as follows:

$$\nabla_{i,j}(\rho u) = \frac{1}{2\Delta x_{i,j}}\left\{u_{i+1/2,j}\left(\rho_{i+1,j} + \rho_{i,j}\right) - u_{i-1/2,j}\left(\rho_{i,j} + \rho_{i-1,j}\right) + \left|u_{i+1/2,j}\right|\left(\rho_{i+1,j} - \rho_{i,j}\right) - \left|u_{i-1/2,j}\right|\left(\rho_{i,j} - \rho_{i-1,j}\right)\right\} \tag{21}$$

In the QUICK method, Equation (21) is approximated as follows:

$$\begin{aligned}\nabla_{i,j}(\rho u) = \frac{1}{16\Delta x_{i,j}}\Big\{&u_{i+1/2,j}\left(-\rho_{i+2,j} + 9\rho_{i+1,j} + 9\rho_{i,j} - \rho_{i-1,j}\right) - u_{i-1/2,j}\left(-\rho_{i+1,j} + 9\rho_{i,j} + 9\rho_{i-1,j} - \rho_{i-2,j}\right) \\ &+\left|u_{i+1/2,j}\right|\left(\rho_{i+2,j} - 3\rho_{i+1,j} + 3\rho_{i,j} - \rho_{i-1,j}\right) - \left|u_{i-1/2,j}\right|\left(\rho_{i+1,j} - 3\rho_{i,j} + 3\rho_{i-1,j} - \rho_{i-2,j}\right)\Big\}\end{aligned} \tag{22}$$

where $\nabla_{i,j}$ is the difference operator in the x,z direction, and i,j on the right-hand side denotes the discretization index. These are upstream differences with conservation properties.

## 5. Results of Experimental Analysis of Density Field Around Rectangle Embankment

The visualized image of each embankment and the density field obtained from the brightness values of the image are superimposed in Figures 5–7. The contours seen in the embankment are due to the grease, and there are no problems in the analysis of the behaviors of the density current of each embankment.

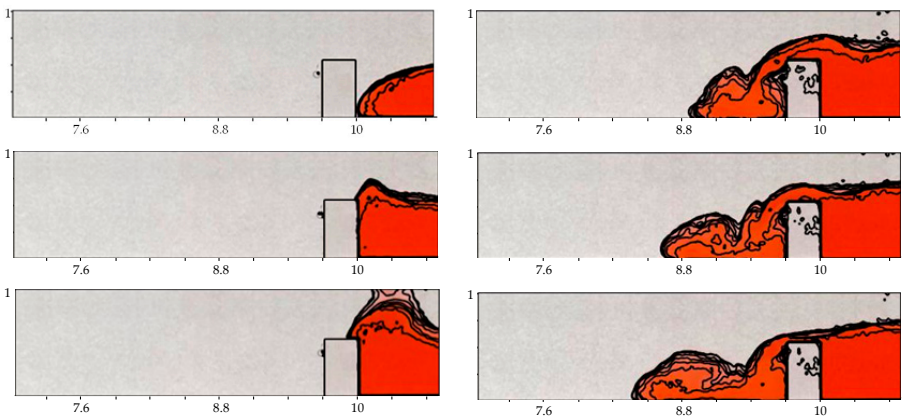


**Figure 5.** *Cont.*

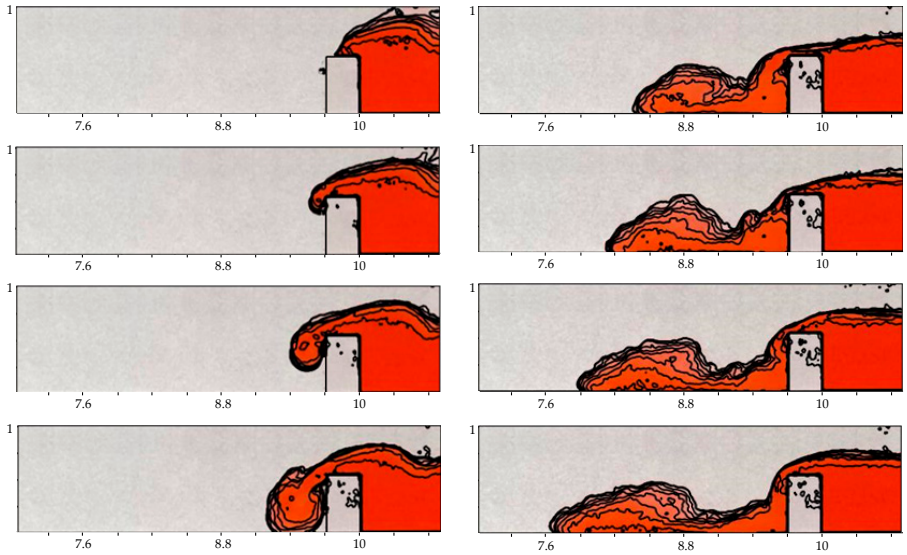


**Figure 5.** Density field around rectangle embankment in the experiment.

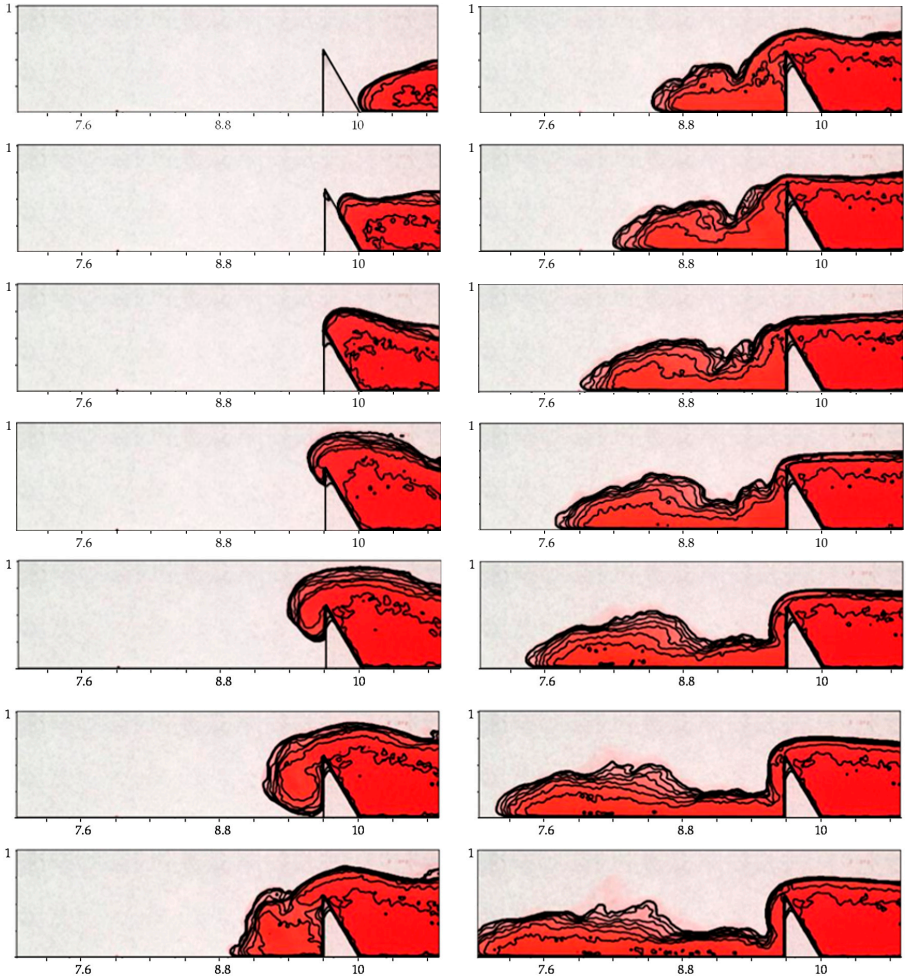


**Figure 6.** Density field around right-angled triangle embankment in the experiment.

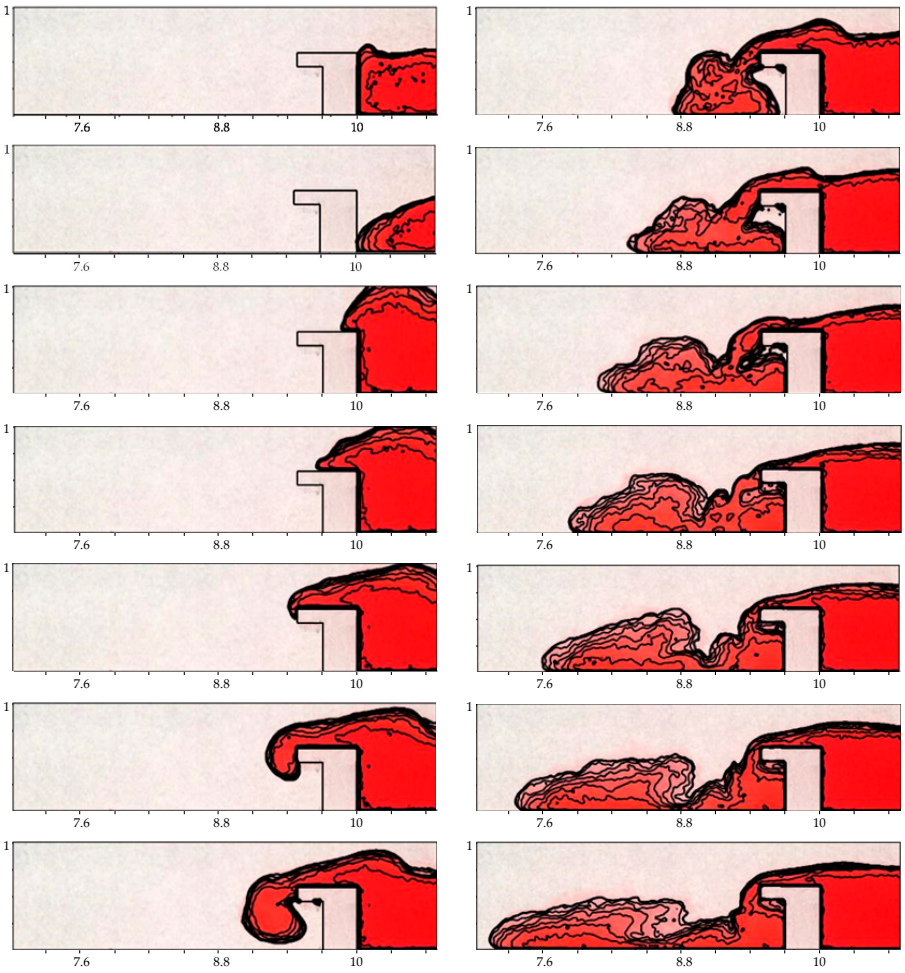


**Figure 7.** Density field around L-shaped embankment in the experiment.

Figures 5–7 shows the density field when the density current overcomes a rectangle, a right-angled triangle, and an L-shaped embankment in case of the density difference $\Delta\rho/\rho = 0.02$. The contour interval is set to $\rho_s = 0.1$. The time interval of the images is 1 in dimensionless time (t/T).

In Figure 5, when the density current impacts the embankment, the head runs up the embankment. As it rushes up, the distance between the density contours becomes wider, indicating that mixing of the fluid is promoted. The density current rushes up to above the height of the wall surface and, when it reaches its maximum, collapses in the direction of travel and in the opposite direction. The head position progresses along the top surface of the embankment, and the thickness of the head becomes thinner. At the same time, reflected waves propagating in the opposite direction of travel are generated. The head reaches the left-hand edge of the embankment top surface and falls, spreading radially. As it falls, the density contours widen, indicating that mixing of the fluid is accelerated. When the head collides with the bottom of the tank, the fluid forms a slightly pointed and rounded head in the direction of travel, while splitting in the left and right directions. The formation of such a head is considered to be due to the Kelvin–Helmholtz instability. The formed head is stretched in the direction of travel as it progresses. At the same time, the head spreads in the vertical upward direction, mixing with the surrounding fluid as it progresses. Figure 6 shows that, similarly for right-angled triangular embankments, when the density current runs up the embankment, the spacing between density contours is wider, but the spread is smaller, and the density diffusion is smaller than for rectangular embankments. In addition, the maximum run-up height is smaller, and the reflected waves due to the embankment are also smaller. After falling from the apex, the head forms and

progresses in the same way as for the rectangular embankment. The shape of the head is the same in each case, but the area of higher density is wider in the case of right-angled triangular embankments than in the other cases. This is considered to be due to the fact that the density diffusion due to the embankment is smaller in the case of right-angled triangular embankments than in the case of other embankment shapes and that the effect of reflected waves due to right-angled triangular embankments is smaller.

Figure 7 shows that the wall on the right side of the rectangular embankment in the L-shape has the same shape, so the density field when running up the wall is the same. The behavior on the top surface of the embankment is also the same, but the head is thinner and flatter due to the greater length of the top surface. The head reaching the left edge of the embankment top surface and falling down while spreading radially is the same as in the case of the rectangular embankment. When the head falls and collides with the tank bottom, the fluid splits in the left–right direction and in the opposite direction to form a rounded semi-elliptical head tapering in the direction of travel. The formed head has a larger contour width and greater density diffusion than the rectangular embankment. This is considered to be due to the fact that the L-shaped embankment has a longer top surface than the rectangular embankment, which increases the velocity of the density current in the direction of travel when it falls and the energy dissipation of the flow in the direction of the embankment due to the accumulation of the flow in the depression of the L-shaped embankment.

## 6. Numerical Results

### *6.1. Comparison of Density Fields*

Figures 8–10 show the density field when the density current overcomes a rectangle, a right-angled triangle, and an L-shaped embankment in case of the density difference $\Delta\rho/\rho = 0.02$. The time interval for each image is 1 in dimensionless time.

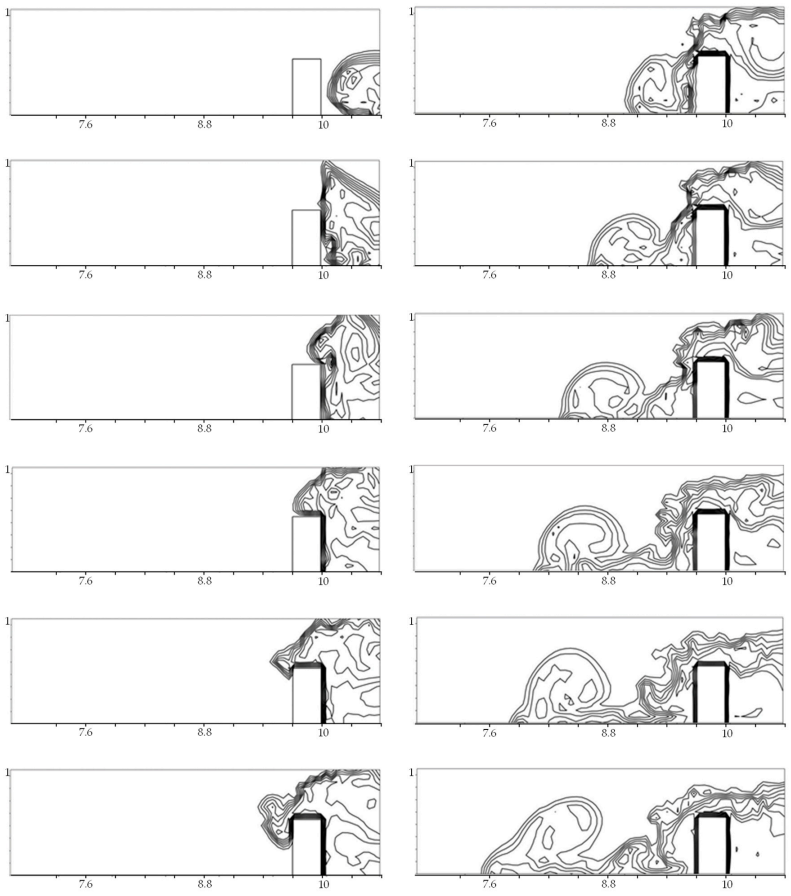


**Figure 8.** *Cont.*

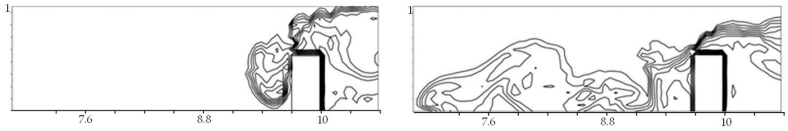


**Figure 8.** Density field near a rectangular embankment in the simulation.

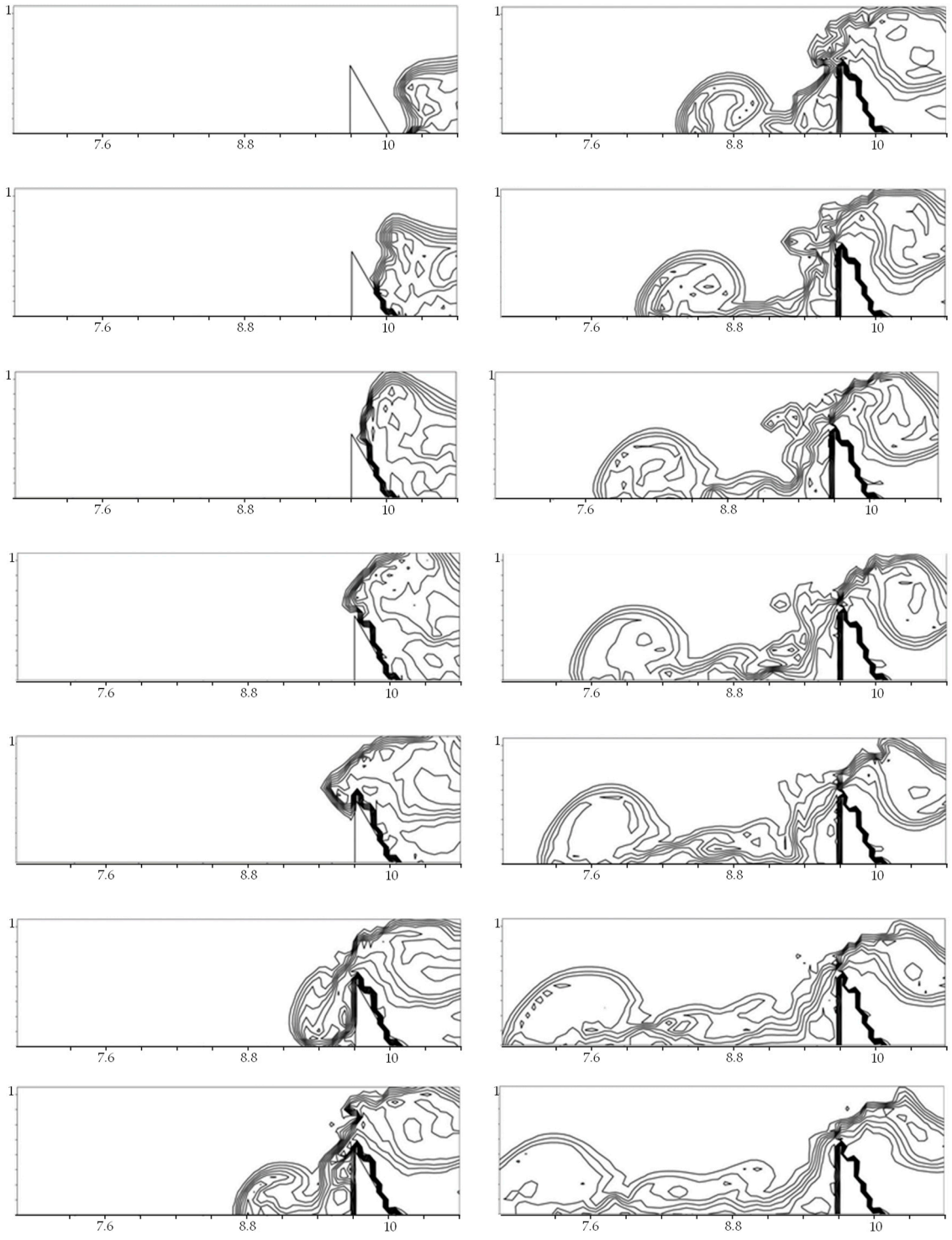


**Figure 9.** Density field near a right-angled triangular embankment in the simulation.

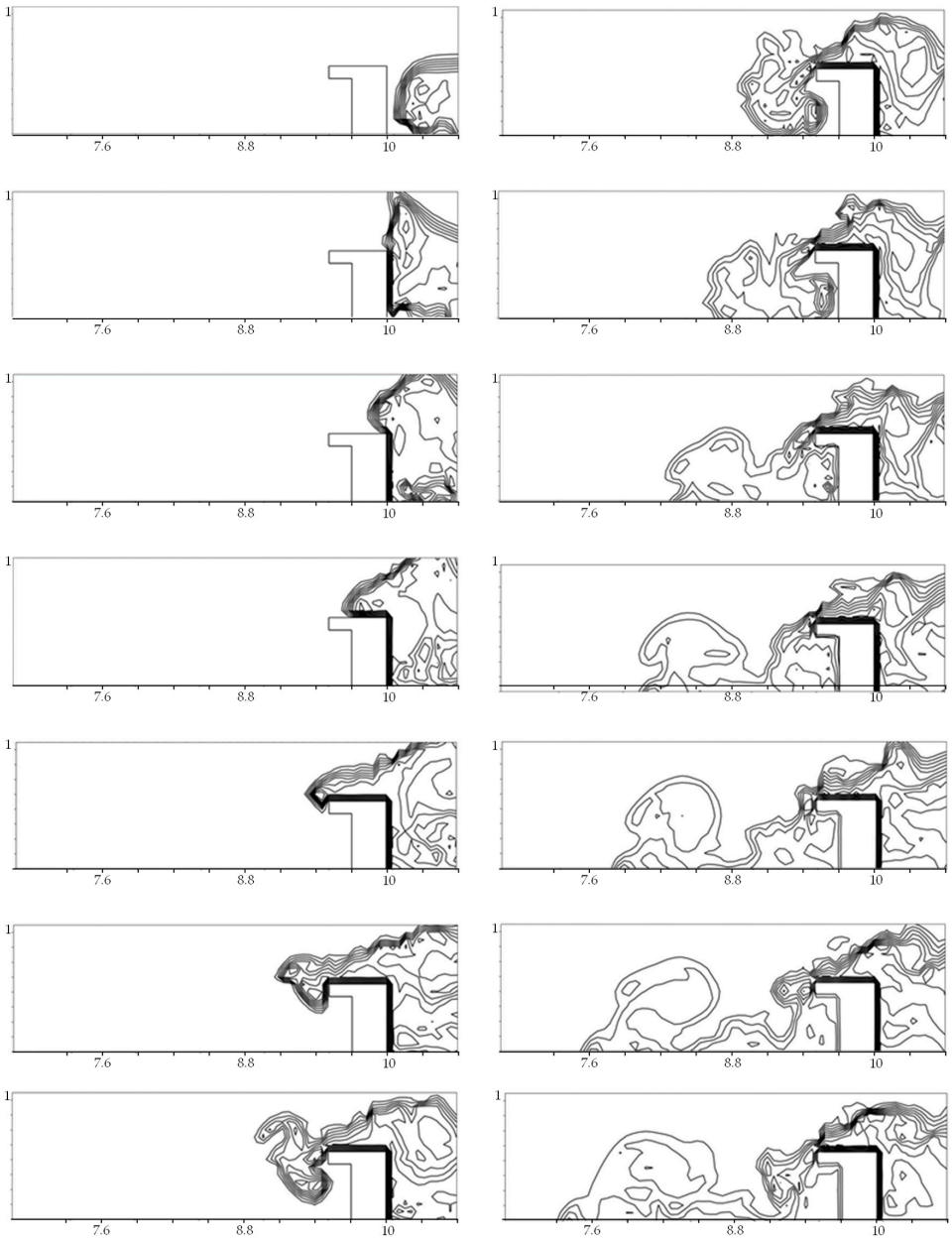


**Figure 10.** Density field near L-shaped embankment in the simulation.

In Figure 8, the density current impacts the embankment, and the head of the embankment runs up along the wall. At the same time, reflected waves propagating in the opposite direction are generated. The object falls radially from the left edge of the top of the embankment. As it falls, the density contours spread. When the head collides with the bottom of the tank, it forms a rounded head shape that is slightly pointed in the direction of travel. The formed head is stretched as it progresses. These behaviors are consistent with experimental results. The width of the density contours of the heads is also consistent with the experimental results, being smaller for right-angled triangular embankments (Figure 9) and larger for L-shaped embankments (Figure 10).

### *6.2. Velocity Field Analysis*

Figures 11–13 shows the velocity field when the density current overcomes a rectangle, a right-angled triangle and an L-shaped embankment in case of the density difference $\Delta\rho/\rho = 0.02$. The time interval for each image is 1 in dimensionless time. Figure 11 shows that the head is traveling in the direction of travel before impacting the embankment, diffusing

vertically with a dimensionless velocity of 0.4. After impacting an embankment, the head position rises in the vertical direction with a dimensionless velocity of 0.5 and 0.6. When the head reaches its maximum height and collapses, the non-dimensional velocity along the top of the embankment in the direction of travel is 0.3, which is greater than in the experiment. At this time, the head also collapsed on the opposite side, and a clockwise vortex was generated as it collapsed. After the head reaches the left edge of the top surface of the embankment, it flows down, spreading radially. After the head impacts the bottom of the tank, the vortex on the upper side forms the head structure. The vortex formed on the lower side collides with the embankment wall and merges with the mainstream of the flowing down fluid.

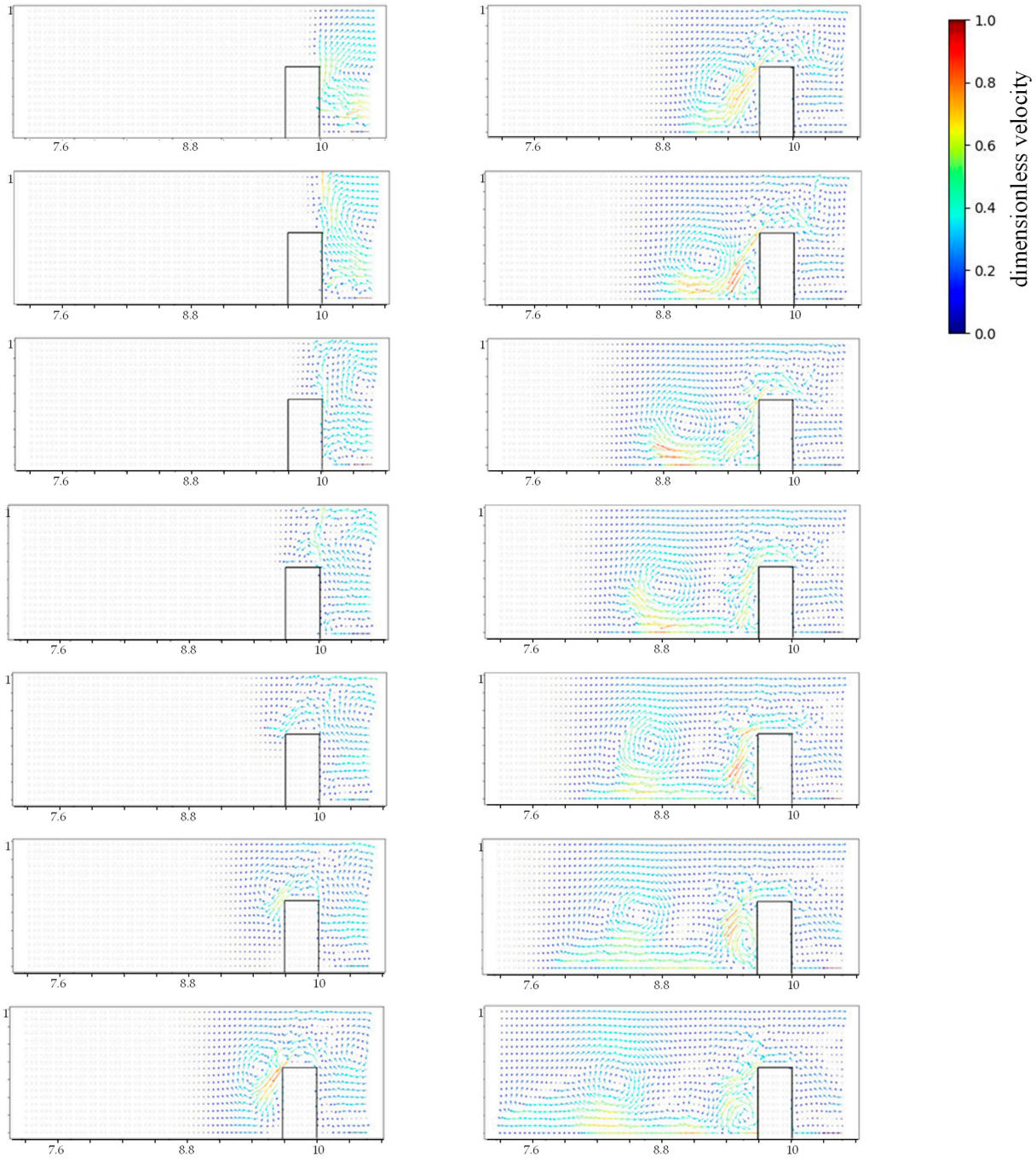


**Figure 11.** Velocity field of density current around a rectangular embankment in the simulation.

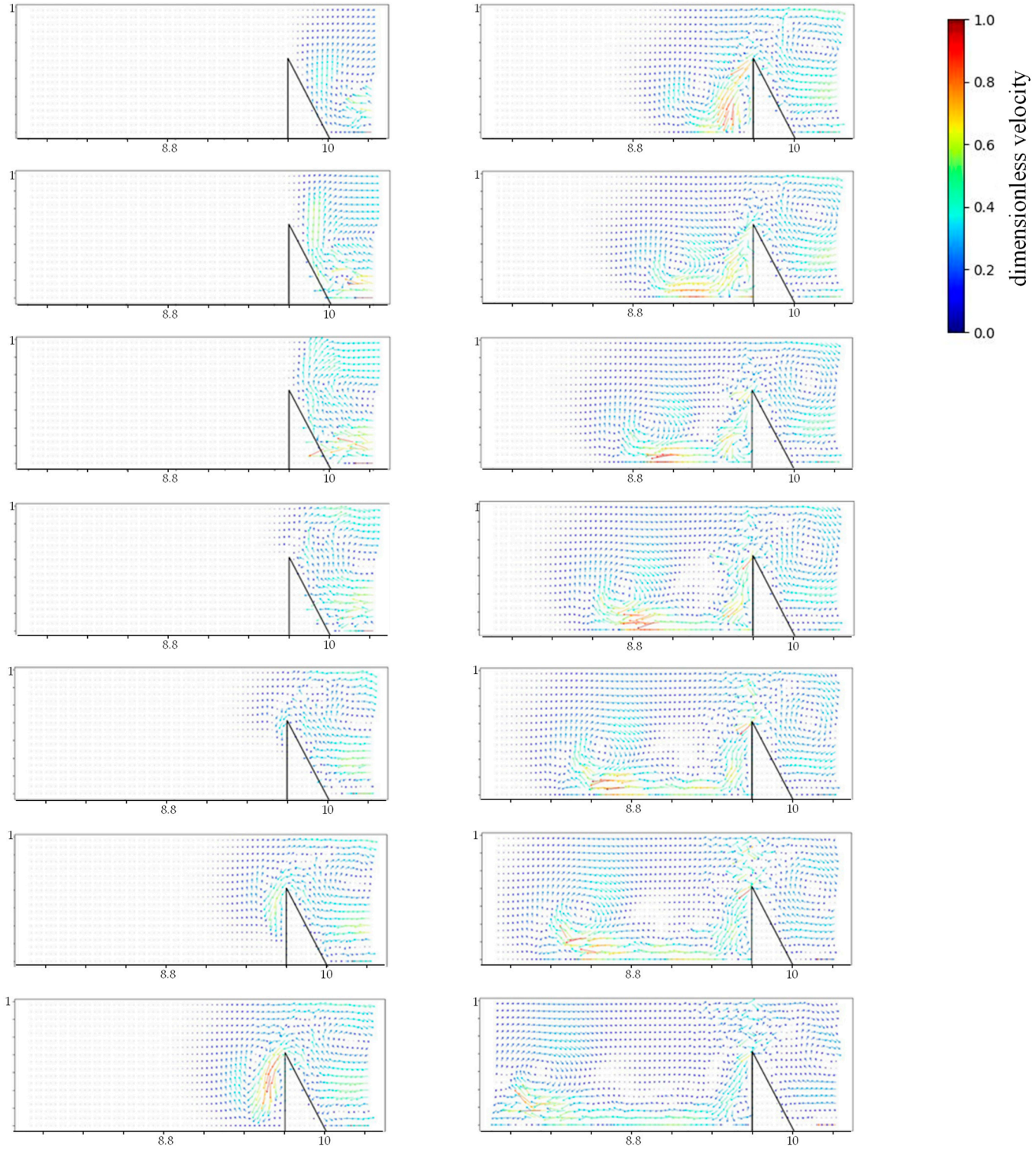


**Figure 12.** Velocity field of density current around a right-angled triangular embankment in the simulation.

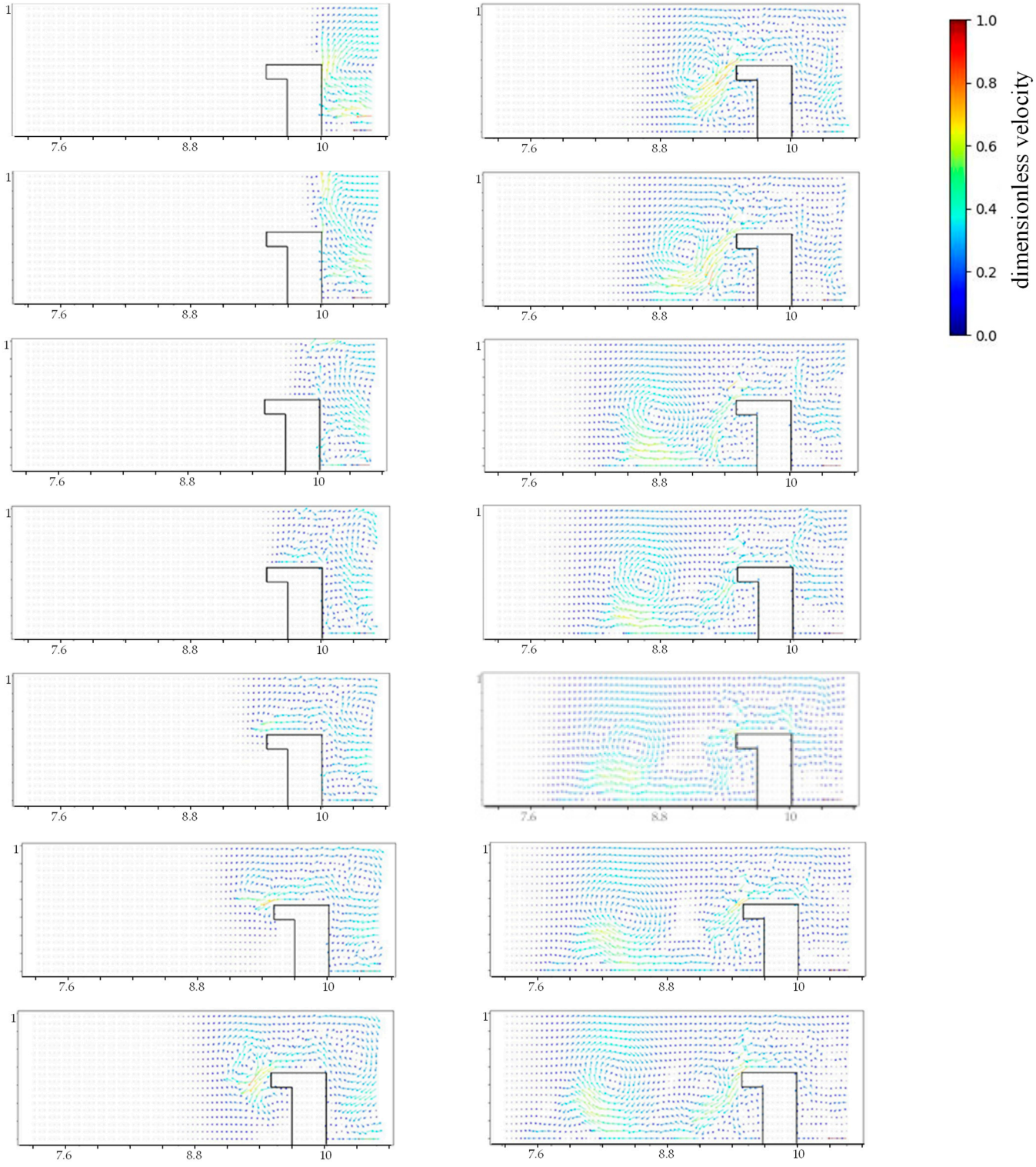


**Figure 13.** Velocity field of density current around an L-shaped embankment in the simulation.

In the case of a right-angled triangular embankment, the head of the vortex impacts the embankment, rushes up, and then forms a clockwise vortex behind the embankment (Figure 12). In the case of an L-shaped embankment, the lower vortex enters the hollow of the L-shaped embankment, weakening its momentum (Figure 13).

### *6.3. Comparison of Head Position of Density Current in Each Case Between Experiment and Simulation*

The relationship between head position and time for each shape is shown in Figure 14, in the case of the density difference $\Delta\rho/\rho = 0.02$. The vertical axis represents the dimensionless position, and the horizontal axis represents dimensionless time. The head position is assumed to have a dimensionless density greater than 0.5. At each embankment, the head position progresses at almost the same slope until t/T = 27, and then the head position stops progressing around t/T = 27~30. During this period, the head of the density current collides with an embankment. After the collision with the embankment, the slope of each shape becomes smaller, which indicates that the moving velocity of the head position becomes smaller. At t/T = 48, the head of the L-shaped embankment moves backward and then moves forward with the same slope. The same reason can be attributed to the recession of the head of the rectangular embankment at t/T = 67. In each shape, the head position receded after the head impacted the tank wall.

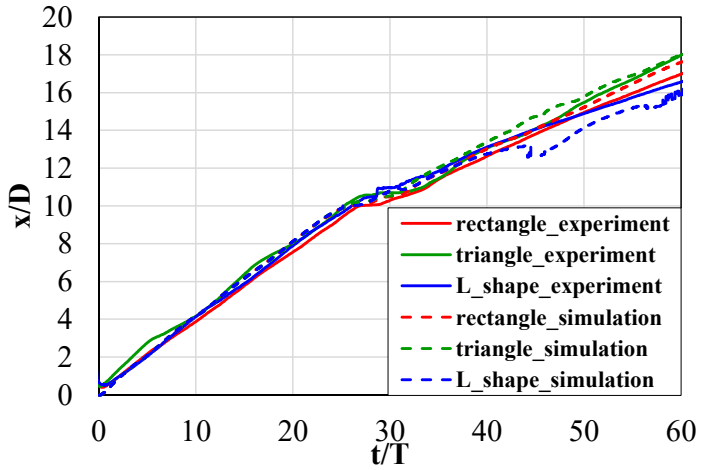


**Figure 14.** Time change of head position of density current in each case of embankment.

As for the simulation, at each embankment, the head position of the density current advanced at the same slope until t/T = 25, and the head position stopped advancing around t/T = 25~30. This was because it collided with an embankment. At t/T = 45, the head of the density current in the case of an L-shaped embankment moved backward and then moved forward with the same slope. These results were consistent with the experimental results, although there was a dimensionless time deviation of 2 to 3.

The dimensionless head velocities for each embankment were examined before and after the embankment impact. Before the embankment impact, the numerically calculated dimensionless head velocity was approximately 0.4 for all embankment shapes. The post-obstacle velocities were 0.236 for the rectangle, 0.239 for the right triangle, and 0.171 for the L-shape. In all shapes, the dimensionless head velocity was smaller than before the embankment impact, and the rate of decrease was particularly large for the L-shaped embankment.

The difference in head velocity between the L-shaped and rectangular obstacles can be attributed to energy dissipation due to vortex generation. Figure 15 shows the average vorticity per lattice per dimensionless time within the analysis range. From Figure 15, it can be seen that the L-shaped embankment has a larger vorticity and greater energy dissipation than the rectangular embankment. This may be due to the fact that when the head falls off the embankment, the vorticity is increased due to the newly formed head.

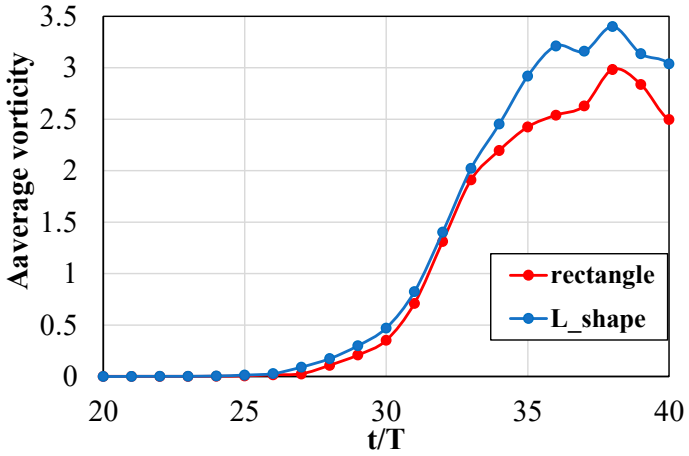


**Figure 15.** The average vorticity per lattice per dimensionless time in the case of a rectangle and L-shape.

## 7. Conclusions

In this study, water tank experiments and numerical calculations were conducted to analyze the flow field of density currents in a channel with different shaped bottom embankments. The shape of embankments was rectangular, L-shaped, and right-angled triangular, and the flow field was analyzed by measuring the density field using the difference in brightness values. Numerical simulations were performed using a two-dimensional finite volume method under the same conditions as in the experiment.

From the density field measurements, when the head of the density current runs up the embankment wall, density diffusion occurs when the head of the density current falls from the top of the embankment, and after falling, when it forms a rounded head that is pointed in the direction of travel, the energy of the density current decreases. Density diffusion is larger for L-shaped embankments and smaller for right-angled triangular embankments, resulting in slower head velocity when L-shaped embankments are installed than when right-angled triangular embankments are installed.

Based on the measurement and numerical calculation of the velocity field method, the velocity is larger when running up the side of the embankment. When the head of the density current falls from the embankment, a counterclockwise vortex is generated on the upper side, and a clockwise vortex is generated on the lower side. This vortex is small for the right triangle embankment and large for the other two embankments. The bottom shape of the water tank (embankment shape) has a large effect on the diffusion velocity of density and the velocity of the head position.

The impact of different embankment geometries on density flow velocities and flow patterns is important in controlling and managing water flows. For example, optimizing bank geometry around rivers and dams can reduce flood risk and promote efficient use of water resources. Proper levee design is expected to protect river, lake, and ocean ecosystems and maintain water quality and aquatic health.

**Funding:** This research received no external funding.

**Data Availability Statement:** The datasets generated and analyzed during the current study are available from the corresponding author on reasonable request.

**Conflicts of Interest:** The author declared that he has no conflicts of interest.

## References

1. Simpson, J.E. *Gravity Currents in the Environment and the Laboratory*, 2nd ed.; Cambridge University Press: Cambridge, UK, 1997.
2. Shin, J.O.; Dalziel, S.B.; Linden, P.F. Gravity currents produced by lock exchange. *J. Fluid Mech.* **2004**, *521*, 1–34. [CrossRef]
3. De Falco, M.C.; Adduce, C.; Negretti, M.E.; Hopfinger, E.J. On the dynamics of quasi-steady gravity currents flowing up a slope. *Adv. Water Resour.* **2021**, *147*, 103791. [CrossRef]

4. Rousso, B.Z.; Bertone, E.; Stewart, R.; Hamilton, D.P. A systematic literature review of forecasting and predictive models for cyanobacteria blooms in freshwater lakes. *Water Res.* **2020**, *182*, 115959. [CrossRef] [PubMed]
5. Iwaki, M.; Yamashiki, Y.; Toda, T.; Jiao, C.; Kumagai, M. Estimation of the Average Retention Time of Precipitation at the Surface of a Catchment Area for Lake Biwa. *Water* **2021**, *13*, 1711. [CrossRef]
6. Issakhov, A.; Zhandaulet, Y. Numerical Study of Technogenic Thermal Pollution Zones' Formations in the Water Environment from the Activities of the Power Plant. *Environ. Model. Asess.* **2020**, *25*, 203–218. [CrossRef]
7. Issakhov, A.; Zhandaulet, Y. Thermal pollution zones on the aquatic environment from the coastal power plant: Numerical study. *Case Stud. Therm. Eng.* **2021**, *25*, 100901. [CrossRef]
8. Wang, Y.; Zheng, X.; Yu, X.; Liu, X. Temperature and salinity effects in modeling the trajectory of the 2011 Penglai 19-3 oil spill. *Mar. Georesour. Geotechnol.* **2017**, *35*, 946–953. [CrossRef]
9. Doronzo, D.M. Aeromechanic analysis of pyroclastic density currents past a building. *Bull. Volcanol.* **2013**, *75*, 684. [CrossRef]
10. Hoult, D.P. OIL Spreading on the sea. *Ann. Rev. Fluid Meach.* **1972**, *4*, 341–368. [CrossRef]
11. Hacker, J.; Linden, P.; Dalziel, S. Mixing in lock-release gravity currents. *Dyn. Atmos. Oceans* **1996**, *24*, 183–195. [CrossRef]
12. Adduce, C.; Sciortino, G.; Proietti, S. Gravity currents produced by lock exchanges: Experiments and simulations with a two-layer shallow-water model with entrainment. *J. Hydraul. Eng.* **2011**, *138*, 111–121. [CrossRef]
13. Koue, J. Effect of bottom wall friction on the transition of developmental stages of gravity current. *Int. J. GEOMATE* **2023**, *24*, 11–117. [CrossRef]
14. Ooi, S.K.; Constantinescu, G.; Weber, L. Numerical simulations of lock-exchange compositional gravity current. *J. Fluid Mech.* **2009**, *635*, 361–388. [CrossRef]
15. Özgökmen, T.M.; Iliescu, T.; Fischer, P.F. Large eddy simulation of stratified mixing in a three-dimensional lock-exchange system. *Ocean Model.* **2009**, *26*, 134–155. [CrossRef]
16. Koue, J. Effect of wall friction on oscillation of velocity at the head of the gravity current. *Theor. Appl. Mech. Lett.* **2023**, *13*, 100439. [CrossRef]
17. Wang, Y.; Yin, Z.; Qiu, Q.; Yang, G.; Yin, D. Numerical study of wave run-up on sea dikes with vegetated foreshores. *Phys. Fluids* **2024**, *36*, 057114. [CrossRef]
18. Neshamar, O.E.; Jacobsen, N.G.; van der A, D.A.; O'Donoghue, T. Linear and nonlinear frequency-domain modelling of oscillatory flow over submerged canopies. *J. Hydraul. Res.* **2023**, *61*, 668–685. [CrossRef]
19. Han, D.; He, Z.; Lin, Y.T.; Wang, Y.; Guo, Y.; Yuan, Y. Hydrodynamics and sediment transport of downslope turbidity current through rigid vegetation. *Water Resour. Res.* **2023**, *59*, e2023WR034421. [CrossRef]
20. Poynton, C.A. *Digital Video and HDTV: Algorithms and Interfaces*; Morgan Kaufmann: San Francisco, CA, USA, 2003; p. 88.